

# We are IntechOpen, the world's leading publisher of Open Access books Built by scientists, for scientists

6,900

Open access books available

185,000

International authors and editors

200M

Downloads

Our authors are among the

154

Countries delivered to

TOP 1%

most cited scientists

12.2%

Contributors from top 500 universities



WEB OF SCIENCE™

Selection of our books indexed in the Book Citation Index  
in Web of Science™ Core Collection (BKCI)

Interested in publishing with us?  
Contact [book.department@intechopen.com](mailto:book.department@intechopen.com)

Numbers displayed above are based on latest data collected.  
For more information visit [www.intechopen.com](http://www.intechopen.com)



## A Wavelet Multiscale De-Noising Algorithm Based on Radon Transform

Xueling Zhu<sup>1,\*</sup>, Xiaofeng Yang<sup>2,\*</sup>, Qinwu Zhou<sup>3</sup>,  
Liya Wang<sup>4</sup>, Fulai Yuan<sup>5</sup> and Zhengzhong Bian<sup>3</sup>

<sup>1</sup>*The School of Humanities and Social Sciences,  
National University of Defense Technology, Changsha,*

<sup>2</sup>*Department of Radiation Oncology, Emory University, Atlanta, GA*

<sup>3</sup>*Department of Biomedical Engineering, School of Life Science and Technology,  
Xi'an Jiaotong University, Xi'an, Shaanxi,*

<sup>4</sup>*Department of Radiology and Imaging Sciences, Emory University, Atlanta, GA,*

<sup>5</sup>*Department of Stomatology, Xiangya Hospital, Central South University, Changsha,*

<sup>1,3,5</sup>*China*

<sup>2,4</sup>*USA*

### 1. Introduction

The rapid development of medical imaging technology and the introduction of new imaging modalities, call for new image processing methods which include specialized noise filtering, enhancement, classification and segmentation techniques. Denoising is a particularly delicate and difficult task in medical images. A tradeoff between noise reduction and the preservation of actual image features has to be made in a way that enhances the diagnostically relevant image content [1].

Single scale filtering methods, like linear (Wiener) or nonlinear (median) are commonly used to eliminate noise. They do not take into account different noise levels and count distributions. Linear filters can reduce the noise variance increasing the signal-to-noise ratio (SNR). However, they smooth images to the point of degrading the image contrast and detail. Nonlinear filters also reduce the noise variance, while preserving the edges to some extent, but image contrast and detail degradation still occurs. In order to avoid such problem many edge preserving filters, like the Anisotropic Diffusion (AD) Filter [2, 3] have been used. Such filters respect edges by averaging pixels in the orthogonal direction of the local gradient. More recently, the trilateral filter [4], an evolution of the bilateral filter [5], has been proposed to take into account local structure in addition to intensity and geometric features.

On the other hand, multiscale filtering methods have also been proposed for image filtering. Unlike single scale filtering methods, multiscale expansions offer the possibility of separating features of interest and noise components into distinct sub-band coefficients.

---

\* Yang X. and Zhu X. contributed equally as co-first authors.

Specifically, multiscale methods, based on wavelet transforms, have widely been applied for noise reduction in medical images. Among the wavelet-based noise reduction techniques, nonlinear thresholding is simple yet very effective. Healy et al. [6] were the first to apply wavelet techniques, based on soft thresholding, for filtering MR images. Nowak [7] squared the magnitude MR image and used a wavelet-based Wiener-filter-like filtering method. Donoho [8] showed a universal threshold of asymptotically optimal in the minimax sense, but it is well-known that the universal threshold over-smoothes images. Pan et al. [9] presented a hard threshold with a nonorthogonal wavelet expansion. At the same time the correlation between wavelet coefficients in several scales has also been employed to filter. Paul et al. [10] presented a multiscale thresholding scheme that incorporated the merits of interscale dependencies into the thresholding technique for filtering, and then applied thresholding to the multiscale products instead of the wavelet coefficients. The interscale correlation information is exploited by Pizurica et al. [11] to classify the wavelet coefficients. Xu et al. [12] developed a spatially selective filtering technique by iteratively selecting edge pixels in the multiscale products. Zhang et al. [13] used Radon transform and an adaptive median filter based on Walsh list in the Laplacian pyramid domain to denoise medical image. These methods are effective for noise suppression. However, there are some significant problems such as blurring, losing of detail texture, the changing of edge points, and generating artificial smear.

In this paper we present a medical image filtering method based on the Radon and wavelet transforms. We perform Radon transform for input images to get sinograms. Then we apply 1D non-orthogonal wavelets transform along  $s$  in sinograms, and use threshold-based methods to filter it. Dissimilar to the traditional threshold schemes that apply the same threshold to the wavelet coefficients at every scale, the proposed method can get robust and adaptive noise threshold at every scale. We can take advantage of the interscale dependency information between wavelet scales to evaluate original noise variance. Finally we apply the inverse Radon transform algorithm to reconstruct the original images. Our method has been validated using MR images. The detailed steps of our method and its evaluative results are reported in the following sections.

## 2. Materials and methods

### 2.1 Radon transform

The Radon transform of a 2D function is defined as:

$$Rf(\alpha, s) = \int_{-\infty}^{\infty} \int_{-\infty}^{\infty} f(x, y) \delta(s - x \cos \alpha - y \sin \alpha) dx dy \quad \alpha \in [0, \pi] \quad s \in R \quad (1)$$

where  $s$  is the perpendicular distance of a line from the origin and  $\alpha$  is the angle formed by the distance vector. Fourier slice theorem states that for a 2D function  $f(x, y)$ , the 1D Fourier transforms of the Radon transform along  $s$ , are the 1D radial samples of the 2D Fourier transform of  $f(x, y)$  at the corresponding angles [14].

#### 2.1.1 Noise robustness

Since the Radon transform is a line integral of the image, the Radon transform of noise is constant for all of the points and directions and is equal to the mean value of the noise.

Therefore, this means zero-mean noise has no effect on the Radon transform of the image. Here we suppose the image is a square with side length  $m = \sqrt{2}a$  ( $a > 0$ ), where  $a$  is the half diagonal length of the square area in terms of pixels. We add up intensity values of the pixels to calculate the Radon transform as shown in Fig. 1. Suppose  $f(x,y)$  is a 2D discrete image whose intensity values are random variables with mean  $\mu$  and variance  $\sigma^2$ . For each point of the projection  $p_s$ , we add up  $n_s$  pixels of  $f(x,y)$ . Therefore,  $var(p_s) = n_s \cdot \sigma^2$ ,  $mean(p_s) = n_s \cdot \mu$ , and  $n_s = 2(a-s)$ , and the integer  $s$  is the projection index, which varies from  $-a$  to  $a$ .

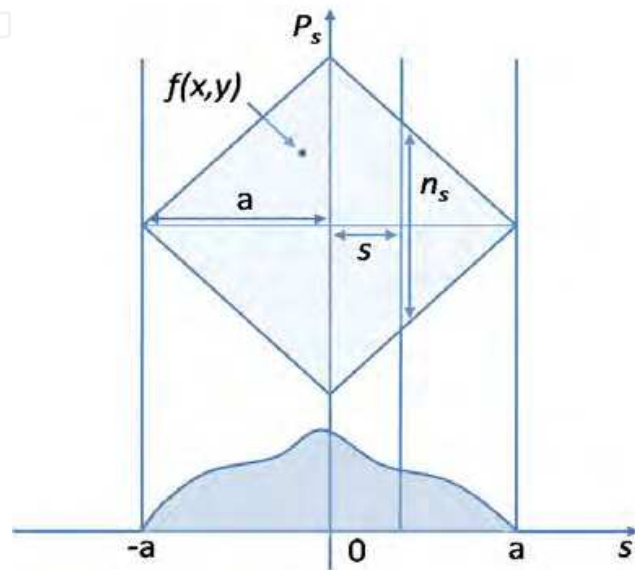


Fig. 1. Diagram for calculations in the Radon domain

The average of  $p_s^2$  is

$$A(p_s^2) = \frac{1}{2a} \sum_{s=-a}^a p_s^2 \tag{2}$$

Its expected value is defined as  $E_p = E\{A(p_s^2)\}$ . Then,

$$E_p = \frac{1}{2a} \sum_{s=-a}^a E\{p_s^2\} = \frac{1}{2a} \sum_{s=-a}^a [var(p_s) + (E(p_s))^2] = \frac{1}{2a} \sum_{s=-a}^a (n_s \sigma^2 + n_s^2 \mu^2) \tag{3}$$

For large  $a$  we can write equation (3) as

$$E_p = \frac{1}{2a} \int_{-a}^a (n_s \sigma^2 + n_s^2 \mu^2) ds \tag{4}$$

So

$$E_p = \frac{1}{a} \int_0^a (2(a-s)\sigma^2 + 4(a-s)^2 \mu^2) ds \tag{5}$$

$$E_p = \frac{2}{a} \int_0^a (2u^2s^2 - (\sigma^2 + 4a\mu^2)s + a\sigma^2 + 2\mu^2a^2) ds \quad (6)$$

$$E_p = \left(\frac{4u^2s^3}{3a}\right) \Big|_0^a - (\sigma^2 + 4a\mu^2) \frac{s^2}{a} \Big|_0^a + (a\sigma^2 + 2\mu^2a^2) \frac{2s}{a} \Big|_0^a$$

$$E_p = a\sigma^2 + \frac{4}{3}a^2\mu^2 \quad (7)$$

From equation (7) we can get  $E_s = a\sigma_s^2 + \frac{4}{3}a^2\mu_s^2$  for the signal, and get  $E_n = a\sigma_n^2$  for white noise with zero mean and variance  $\sigma_n^2$ . Then,

$$SNR_{Radon} = \frac{E_s}{E_n} = \frac{\sigma_s^2}{\sigma_n^2} + \frac{4a}{3} \cdot \frac{\mu_s^2}{\sigma_n^2} \quad (8)$$

In original image we define  $SNR_{image} = (\sigma_s^2 + \mu_s^2) / \sigma_n^2$ . Therefore,

$$SNR_{Radon} = \frac{\sigma_s^2 + \mu_s^2}{\sigma_n^2} + \left(\frac{4a}{3} - 1\right) \cdot \frac{\mu_s^2}{\sigma_n^2} = SNR_{image} + \left(\frac{4a}{3} - 1\right) \cdot \frac{\mu_s^2}{\sigma_n^2} \quad (9)$$

For medical images like MRI or CT the signal is distributed over the whole intensity range we can always get  $\mu_s^2 \geq \sigma_s^2$ , and we may write  $SNR_{image} \leq 2\mu_s^2 / \sigma_n^2$ . Therefore,

$$SNR_{Radon} \geq \left(\frac{4a+3}{6}\right) SNR_{image} = \frac{2\sqrt{2m+3}}{6} SNR_{image} \quad (10)$$

This shows that  $SNR_{Radon}$  has been increased by a factor of at least  $\frac{2\sqrt{2m+3}}{6}$ , which is in practice much too large a quantity. If the image size is  $256 \times 256$ , and then  $SNR_{Radon} = \frac{2\sqrt{2} \times 256 + 3}{6} \cong 121.2$  or  $(10 \log_{10} 121.2 = 20.8dB)$ .

### 2.1.2 The results for noise reducing

From above, we can see that the Radon transform is very robust in reducing the effect of additive noise. Here we add 3% and 10% Gaussian noise with a zero mean to the original phantom and at the same time we perform the Radon transform to get corresponding sinograms as shown in Fig. 2. Fig. 3(a) shows the profiles through the original image and the noised image (the profile position is shown in the top row of Fig. 2), Fig. 3(b) shows the profiles through their corresponding sinograms (the profile position is shown in the bottom row of Fig. 2). In Fig. 3(a) it is easy to see that the image with 10% noise has already been contaminated severely, and we cannot see any image details in the noised image. In Fig. 3(b) we can clearly see the profiles through the corresponding sinograms are very close, and it

shows the transform has greatly decreased the noise in the original image. Since the Radon transform is a linear transform and is invertible, it does not lose any texture information. And rotation of the input image corresponds to the translation of the Radon transform along  $\alpha$ , which is more tractable.

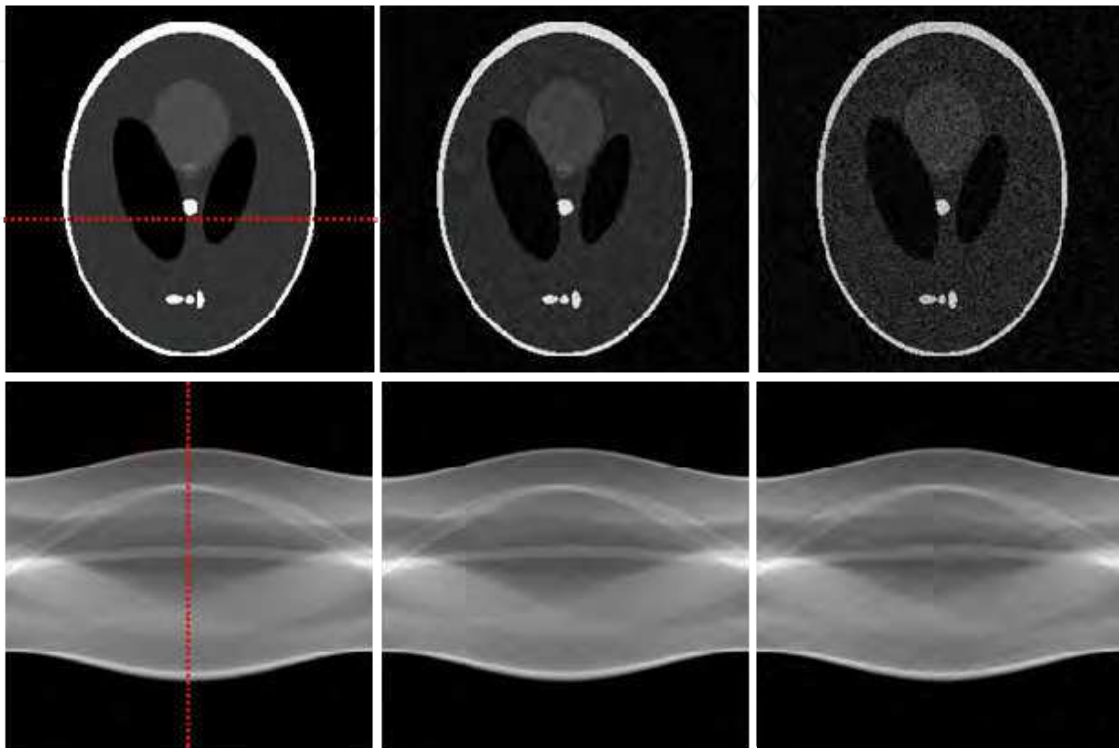


Fig. 2. Phantoms and corresponding sinograms. The top row consists of phantoms without noise and with 3% and 10% noise respectively. The bottom row is the corresponding sinograms of the top row phantoms.

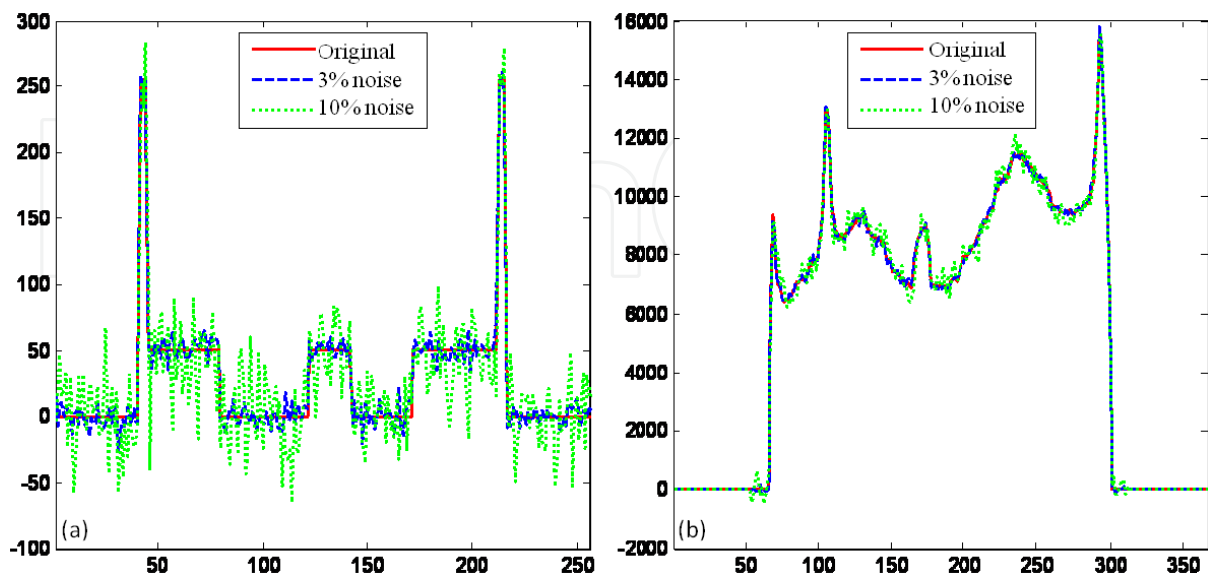


Fig. 3. Quantitative comparison of profiles through images. (a) The profiles between the original and the noised images. (b) The profiles of the corresponding sinograms.

## 2.2 Wavelet transform

### 2.2.1 Wavelet theory

Wavelets are mathematical functions that decompose data into different frequency components. Then each component is performed with a resolution matched to its scale [15]. The wavelet analysis decomposes a signal into a hierarchy of scales ranging from the coarsest scale to the finest one. Hence, wavelet transforms which provide representation of an image at various resolutions are a better tool for feature extraction from images. Wavelet coefficients of a signal are the projections of the signal onto the multiresolution subspaces. Wavelets are functions generated from basis function, called the mother wavelet, by dilations and translations in time (frequency) domain. If the mother wavelet is denoted by  $\psi(t)$  other wavelets  $\psi_{A,B}(t)$  can be represented as

$$\psi_{A,B}(t) = 1 / \sqrt{|A|} * \psi((t - B) / A) \quad (11)$$

where  $A$  and  $B$  are two arbitrary real numbers. The variables  $A$  and  $B$  represent the parameters for dilations and translations respectively in the time axis.

### 2.2.2 Dyadic wavelet transform

The discrete wavelet transform is an implementation of the wavelet transform using a discrete set of the wavelet scales and translation which obey some defined rules. For practical computations, it is necessary to discretize the wavelet transform. The scale parameter  $A$  is discretized on a logarithmic grid. The translation parameter  $B$  is then discretized with respect to the scale parameter, i.e. sampling is done on the dyadic sampling grid. A dyadic wavelet transform is a semi-discrete wavelet transform, makes scale factor binary discrete, but the displacement factor to change continuously. The discretized scale and translation parameters are given by  $A = 2^{-j}$  and  $B = k2^{-j}$ , where  $j, k \in Z$ , is the set of all integers. Thus, the family of wavelet functions is represented as

$$\psi_{j,k}(t) = 2^{j/2} \psi(2^j t - k) \quad (12)$$

When analyzing wavelet transforms from a multiresolution point of view, the wavelet decomposition of a discrete time signal  $X[n]$  is given by

$$X[n] = \sum_k c_{j_0,k} \varphi_{j_0,k}(n) + \sum_{j=j_0}^{\infty} \sum_k d_{j,k} \psi_{j,k}(n) \quad (13)$$

where  $\varphi_{j_0,k}$ ,  $\psi_{j,k}$  are the scaling functions and wavelet functions respectively.

As shown in Fig. 4, for any coarse scale  $2^j$ , a discrete signal sequence  $\{S_j f, (W_j f)_{1 \leq j \leq J}\}$  is named as the discrete wavelet transform of the original signal  $f$ . In Fig. 4,  $H_j(G_j)$  is taken for the  $2^j$ th scale expansion of  $H_1(G_1)$ , that is, inserted  $2^j - 1$  zeros among the filter coefficients.

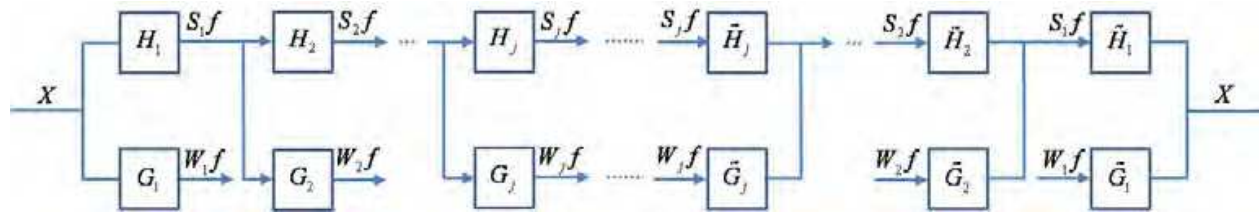


Fig. 4. Dyadic wavelet transforms

Reconstruction is the reverse process of decomposition, so we only need to exchange the decomposition filters for the reconstruction filters. The decomposition and reconstruction of  $f(t)$  is completed by the Mallat tower algorithm [16]. Fast wavelet reconstruction (16) and inverse fast wavelet reconstruction (17) are given below

$$\begin{cases} c_{j,k} = \sum_m h(m-2k)c_{j+1,m} \\ d_{j,k} = \sum_m g(m-2k)c_{j+1,m} \end{cases} \tag{14}$$

$$c_{j+1,m} = \sum_k c_{j,k}h(m-2k) + \sum_k d_{j,k}g(m-2k) \tag{15}$$

Where  $c$  is the scale factor,  $d$  is the wavelet coefficients, and  $h$  and  $g$  are coefficient of the filter  $H$  and  $G$  respectively in Fig. 4.

**2.2.3 Wavelet base choice**

Orthogonal wavelet transforms have fewer coefficients at coarse scales, and therefore the transformed signal is uncorrelated across the scales. Lack of a translation invariant will make filtering by orthogonal wavelet transforms exhibit visual artifacts. The non-orthogonal wavelet offers much better edge detection because the signal is correlated across the scales. Non-orthogonal wavelet is better than orthogonal wavelet for SNR [9]. In this paper we use non-orthogonal wavelets first introduced by Mallat et al. [17]. This base wavelet is shown in Fig. 5.

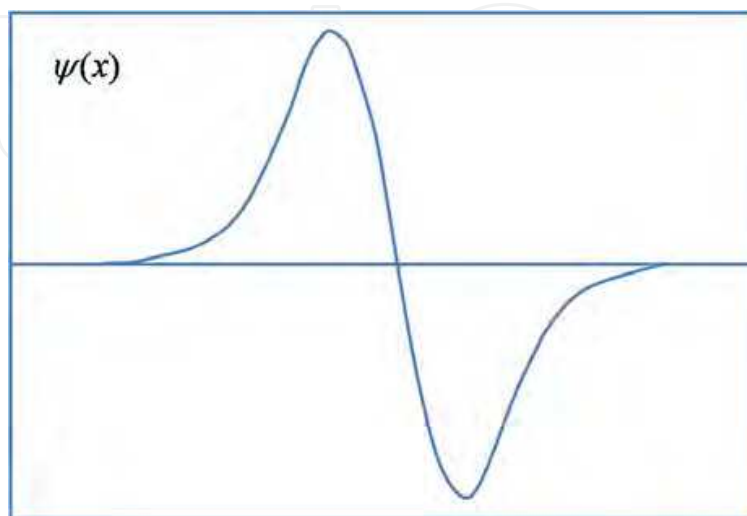


Fig. 5. Plot of a typical quadratic spline wavelet

It is very close to the derivative of a Gaussian function. From the Radon transform, we know the translation along  $\alpha$  in the Radon domain corresponds to the rotation of the input image. The shift along  $s$  in the Radon domain corresponds to the translation of the input image. So we apply a 1D wavelet transform along  $s$ .

### 2.2.4 Threshold-based filtering

Threshold-based filtering is very simple and gives a satisfactory performance. It can be divided into three steps: (1) transform the noisy signal into wavelet coefficient  $w$ , (2) employ a hard or soft threshold  $t_j$  at each scale  $j$ , (3) transform back to the original domain, and get the estimated signal. Although Donoho [8] proved the optimality of a soft threshold in theory, a hard threshold has shown better results for certain applications.

$$\hat{w}(j,n) = \begin{cases} w(j,n) & w(j,n) \geq t_j \\ 0 & w(j,n) < t_j \end{cases} \quad (16)$$

As can be seen from filtering theory, during the wavelet filtering process a small threshold value will leave behind all the noisy coefficients, and subsequently, the resultant filtered image may still be noisy. On the other hand, a large threshold value will make more of the coefficients zero, and the resultant image may be blurred and have artifacts. So the threshold is key to the signal filtering effect, how the threshold is determined is critical. We choose  $t_j = c\sigma_j$ , where  $c$  is a constant. It is well known that for *i.i.d.* Gaussian noise  $X \sim N(0, \sigma^2)$ , a threshold  $t = \sigma, 2\sigma, 3\sigma, \dots$  will suppress 68.26%, 95.44%, and 99.74% of its values. Therefore, imposing  $c$  between 3~4, will give good results.

From the above discussion we can see the choice of threshold depends on the noise variance  $\sigma_j$  in different scales. So the key is how to get the optimum noise variance  $\sigma_j$ , which is adaptive to different scale characteristics [18].

### 2.2.5 Noise variance $\sigma_j$ in different scales

In order to get the noise variance in different scales we suppose white noise is  $\varepsilon$ , its variance is  $\sigma^2$ , the power spectral density (PSD) is  $S_\varepsilon(\omega) = \sigma^2$ . After applying filter  $G_1$  (see Fig. 4) the variance of the wavelet coefficient  $W_1\varepsilon$  is  $\sigma_1^2$ . Suppose

$G_1(\omega) = \sum_{-\infty}^{\infty} g_1(n)e^{-jn\omega}$ , where  $g_1(n)$  is the pulse response sequence, and  $\omega \in [-\pi, \pi]$ , and

then  $S_{W_1}(\omega) = |G_1(\omega)|^2 S_\varepsilon(\omega)$ , Therefore, the autocorrelation function of  $W_1\varepsilon$

is  $R_{W_1}(\tau) = \frac{1}{2\pi} \int_{-\infty}^{\infty} S_{W_1}(\omega) e^{j\omega\tau} d\omega$ . After filtering the mean of white noise is zero.

$$\begin{aligned}
\sigma_1^2 &= R_{W_1}(0) = \frac{1}{2\pi} \int_{-\infty}^{\infty} |G_1(\omega)|^2 S_\varepsilon(\omega) d\omega \\
&= \frac{\sigma^2}{2\pi} \int_{-\pi}^{\pi} \left[ \sum_{n=-\infty}^{\infty} g_1(n) e^{-jn\omega} \right] \left[ \sum_{n=-\infty}^{\infty} g_1(n) e^{jn\omega} \right] d\omega \\
&= \sigma^2 \sum_{n=-\infty}^{\infty} (g_1(n))^2 = \sigma^2 \|g_1\|^2
\end{aligned} \tag{17}$$

In (19)  $\| \cdot \|$  denotes the norm of a vector, so  $\sigma_2^2 = \sigma^2 \|h_1 * g_2\|^2$ , and then

$$\sigma_j^2 = \sigma^2 \|h_1 * h_2 * \dots * h_{j-1} * g_j\|^2 \tag{18}$$

where  $h_j$  and  $g_j$  are the unit pulse response of  $H_j$  and  $G_j$  respectively.  $h$  and  $g$  depend on the scaling function  $\phi(t)$  and wavelet function  $\psi(t)$ . They are not determined by specific scale.

### 2.2.6 Noise variance $\sigma$ estimation

Our algorithms require the calculation of the underlying noise variance  $\sigma$ . In a real world application, the variance is usually unknown a priori, so it must be estimated from the data. Some papers used the dark (signal free) regions at the boundaries of each image to estimate the noise power at each wavelet scale. But this method requires manually choosing such regions and sometimes the noise in medical images is not uniformly distributed in both signal and free regions [19].

Based on [12] we are using the spatial correlation  $Corr_2(j, n)$  between the first two scales of wavelet transform to compute the power of  $P_{corr}(j)$  and  $P_W(j)$

$$P_{corr}(j) = \sum_n Corr_2(j, n)^2 \tag{19}$$

$$P_W(j) = \sum_n W(j, n)^2 \tag{20}$$

$$Corr_2(j, n) = W(j, n) * W(j+1, n) \quad n = 1, 2, \dots, N \tag{21}$$

where  $W(j, n)$  denotes the wavelet transform data. The power of  $Corr_2(j, n)$  is then rescaled to that of  $W_2(j, n)$

$$NewCorr_2(j, n) = Corr_2(j, n) \times \sqrt{P_W(j) / P_{corr}(j)} \tag{22}$$

If  $|NewCorr_2(1, n)| > |W_2(1, n)|$ , then the corresponding data in  $W(1, n)$  is reset to 0. Refer to the remainder of  $W(1, n)$  as  $\tilde{W}(1, n)$ . Suppose  $k$  points are killed totally; then  $\tilde{W}(1, n)$  can be roughly considered to be produced by noise. It is well known that  $\sqrt{P_x / M}$  is an

asymptotically unbiased estimation of  $\sigma$  for a sequence  $X \sim N(0, \sigma^2)$ , where  $P_x = \sum_n x(n)^2$  and  $M$  is the length of  $X$ . From  $\sigma = \sigma_1 / \|g_1\|$  and the asymptotically unbiased estimation of  $\sigma_1^2$ , we can get

$$\sigma = \sqrt{\tilde{P}_W(1)/(N-k-1)} / \|g_1\| \quad (23)$$

From the Radon transform and Fig. 1, the noise variance  $\sigma_{s,j}$  of the  $j$ th scale in the Radon domain is determined as

$$\sigma_{s,j} \approx \|h_1 * h_2 * \dots * h_{j-1} * g_j\| n_s \sqrt{\sigma^2 / (JI)} \quad (24)$$

where  $n_s$  are the pixels through the image as shown in Fig. 1, and  $J$  and  $I$  are the size of the image.

Based on all of the above deductions the adaptive threshold in the Radon domain is given as

$$\begin{aligned} t_{s,j} &= c \cdot \sigma_{s,j} = c n_s \|h_1 * h_2 * \dots * h_{j-1} * g_j\| \sqrt{\sigma^2 / (JI)} \\ &= c n_s \|h_1 * h_2 * \dots * h_{j-1} * g_j\| \sqrt{\tilde{P}_W(1) / [JI(N-k-1)]} / \|g_1\| \end{aligned} \quad (25)$$

This threshold can vary adaptively, because it depends on the decomposed scales and the pixels through image in the Radon transform adaptively.

### 2.3 Inverse radon transform

After obtaining the filtered sinogram, we perform an inverse radon transform in order to get the original image. It is defined as

$$f(x, y) = \int_0^\pi R(\alpha, x \cos \alpha + y \sin \alpha) d\alpha \quad (26)$$

where  $R$  is the filtered projections. Generally, three different inverse Radon transform methods are direct inverse Radon transform (DIRT), filtered back-projection (FBP) and convolution filtered back-projection (CFBP) [20]. DIRT is computationally efficient, but it introduces some artifact. FBP based on linear filtering model often exhibits degradation in recovering from noisy data [21]. Spline-convolution filtered back-projection (SCFBP) offers better approximation performance than the conventional lower-degree formulation (e.g. piecewise constant or piecewise linear models) [22]. For SCFBP the denoised sinogram in the Radon domain is approximated in the B-spline space, while the resulting image in image domain is in the dual-spline space. We used SCFBP to propagate the denoised sinogram back into the image space along the projection paths.

## 3. Experiments and results

Our filtering method has been evaluated by using simulation brain data. We also applied the method to filter real brain MR images. Single scale optimum linear filter - Wiener filter,

traditional multiscale wavelet filter [8], anisotropic diffusion (AD) filter [2, 3] and bilateral filter [5, 25] were applied to these dataset in order to compare the performance of these filtering methods. Here we define an average SNR as quality metric. It is given by

$$SNR = 10 \log_{10} \frac{\sum_{m,n} |X[m,n]|^2}{\sum_{m,n} |X[m,n] - \hat{X}[m,n]|^2} \quad (27)$$

with the results averaged over all images and reported as mean decibels ( $dB$ ), where  $X[m,n]$  is the original image and  $\hat{X}[m,n]$  is the filtered image.

We transformed the intensity of all testing images to uint8 (0~255) before all images were filtered with the five methods. Neighborhoods of size  $3 \times 3$  were used to estimate the local image mean and standard deviation of Wiener filter. A Db3 wavelet was used in the traditional wavelet filter, and the images were decomposed to four levels. The constant was imposed  $c = 3.78$  in our method, and the images were also decomposed to four levels. For simulated and real brain data the AD filter was used when diffusion constant was 140. And the bilateral filter was performed when spatial function variance  $\sigma_s = 3$ , range function variance  $\sigma_r = 20$ .

### 3.1 Simulation brain MR data

We obtained the brain MR images from the McGill phantom brain database for comprehensive validation of the different filtering methods. The MR volume was constructed by subsampling and averaging a high-resolution (1-mm isotropic voxels) dataset consisting of 27 aligned scans from one individual in the stereotaxic space. The volume contains  $181 \times 217 \times 181$  voxels and covers the entire brain. Based on the realistic phantom, an MR simulator is provided to generate specified MR images [23].

We obtained T1-weighted, T2-weighted and Pd-weighted MR volumes with an isotropic voxel size of 1mm at different noise levels. The noise effect was simulated as zero mean Gaussian noise adding to the MR volume with its standard deviation equal to the noise percentage multiplied by the brightest tissue intensity [24, 26]. Fig. 6 illustrates the visual assessment of filtered results on simulated T1-weighted, T2-weighted and Pd-weighted MR images with 9% noise and the comparison of the five different methods. We can easily see that bilateral filter and our method reduce more noise than other filtering methods. But the results of our method are much closer to original images without noise than those of bilateral filter.

Fig. 7 shows output SNR comparison of different filters for different image types (T1-weighted, T2-weighted and Pd-weighted MR image) and noise levels (1%, 3%, 5%, 7%, 9%, 11%, 13%, 15% and 17%). The output SNRs of the five methods for three types of MR images always decrease as the noise in MR image increases, and even some output SNRs of AD filter is less than input SNRs. From the three figures it can be seen that the output SNR of our method is always higher than other methods for almost all noised MR images except Pd-weighted images with 3% and 5% noise. Moreover, output SNRs of all denoising methods are always less than input SNRs of original MR images when original images have been added 1% Gaussian noise. We also see that the more noise (over 11%) exists in MR images, the better our method performs than others.

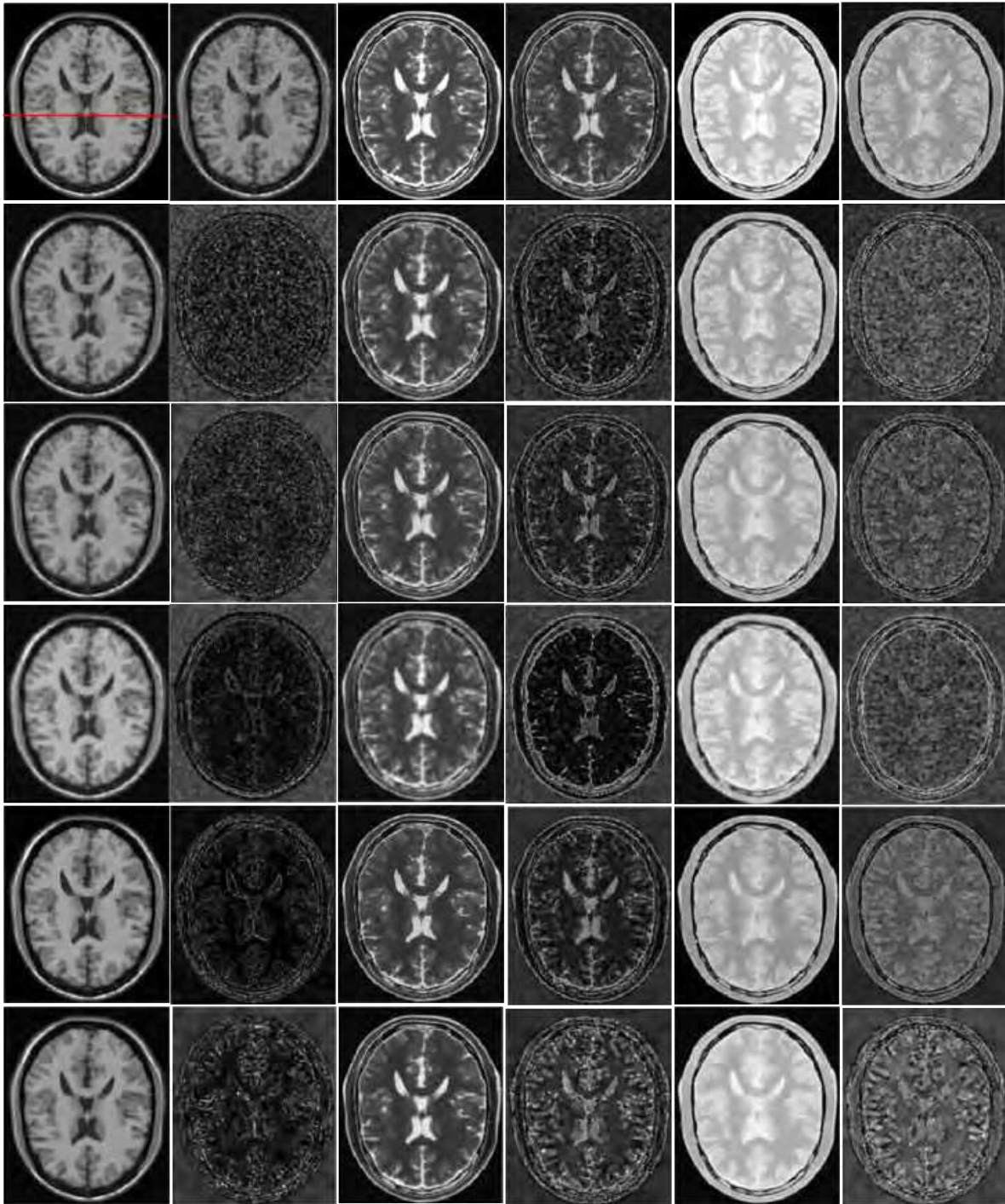
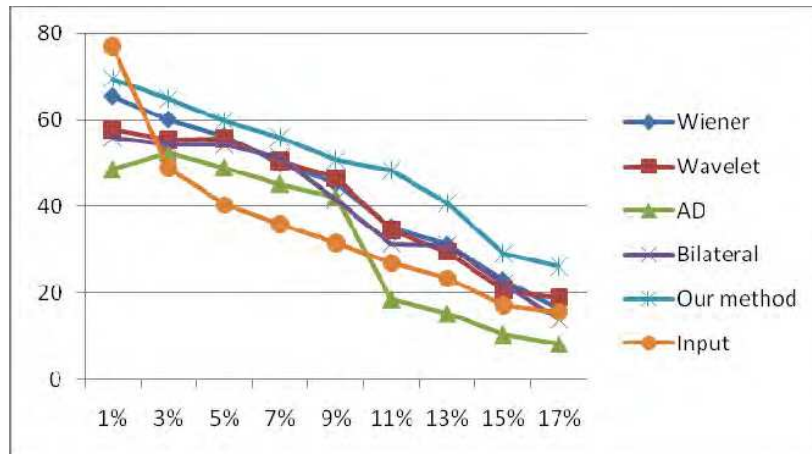
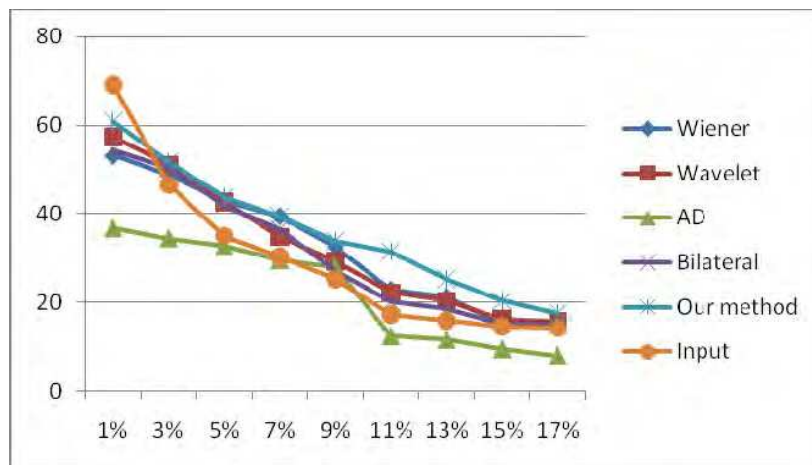


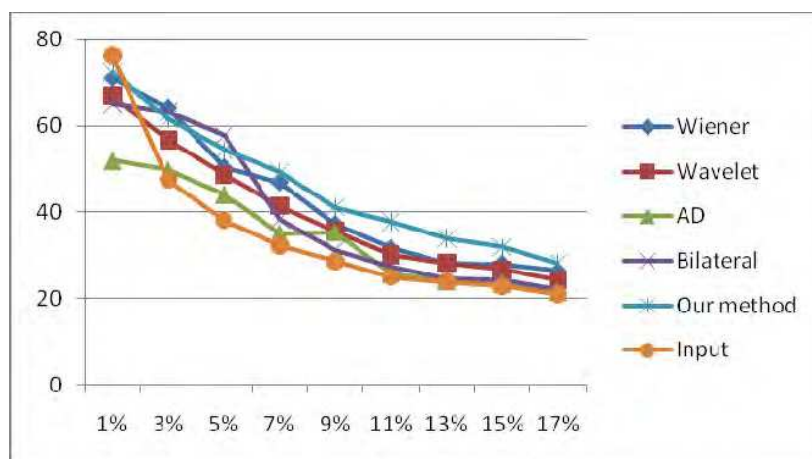
Fig. 6. Filtered results of the simulated brain data. The first row shows original T1-weighted MR image, noised T1-weighted MR image, original T2-weighted MR image, noised T2-weighted MR image, original Pd-weighted MR image and noised Pd-weighted MR image from left to right respectively. The first column shows the T1-weighted filtered results using Wiener filter, wavelet filter, AD filter, bilateral filter and our method from the second row to the bottom respectively. The second column shows the corresponding residuals between the original image and the filtered image. The third and fourth columns are T2-weighted filtered results after using the different methods and the corresponding residuals. And the fifth and sixth columns are the corresponding Pd-weighted results and residuals.



(a) T1-weighted MR image



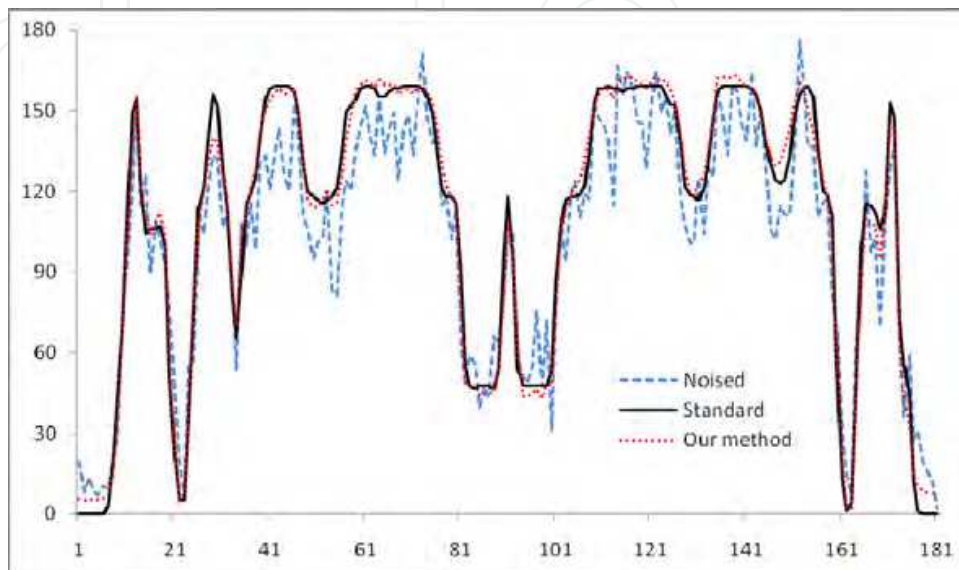
(b) T2-weighted MR image



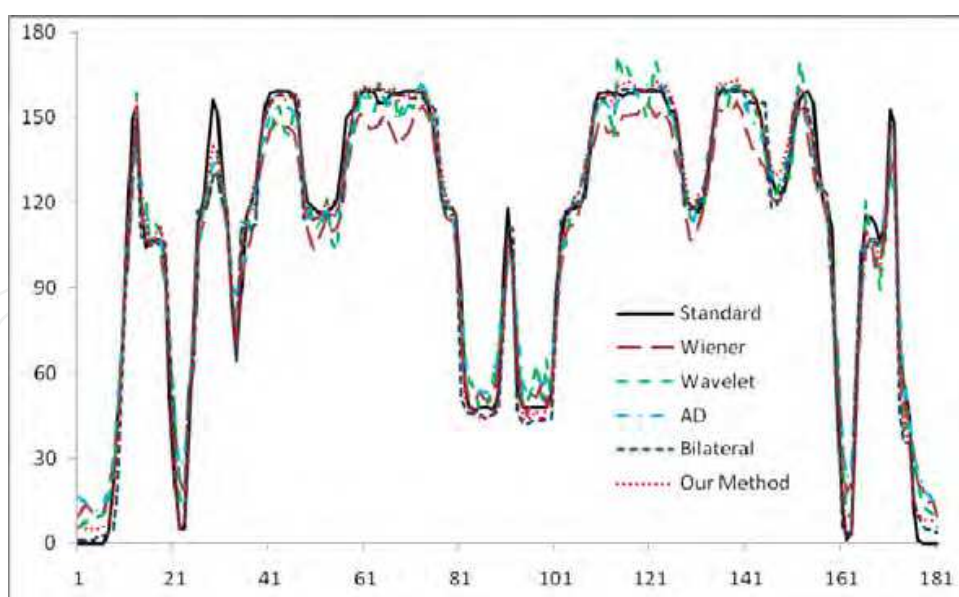
(c) Pd-weighted MR image

Fig. 7. Output SNR comparison of the different filters for different image types and noise levels. In (a), (b) and (c) the horizontal axis is different noise levels. The vertical axis is the output SNRs (dB) of the different filters and the original input SNRs (dB) of different noise levels.

Fig. 8 indicates the quantitative comparison of horizontal profiles between original T1-weighted image and filtered images after using the different methods. The profile position is shown in the original T1-weighted MR image of Fig.6. From Fig.8 we can see that the filtered result of our method is closest to original standard image without noise in all denoised results. It demonstrates our method is effective in reducing noise and preserving details in MR image.



(a) Comparison of horizontal profiles between original standard, noised image and the filtered image after using our method.



(b) Comparison of horizontal profiles between original standard, the filtered images using Wiener filter, wavelet filter, AD filter, bilateral filter and our method respectively.

Fig. 8. Comparison of horizontal profiles between the original T1-weighted image and the filtered images after using the different methods.

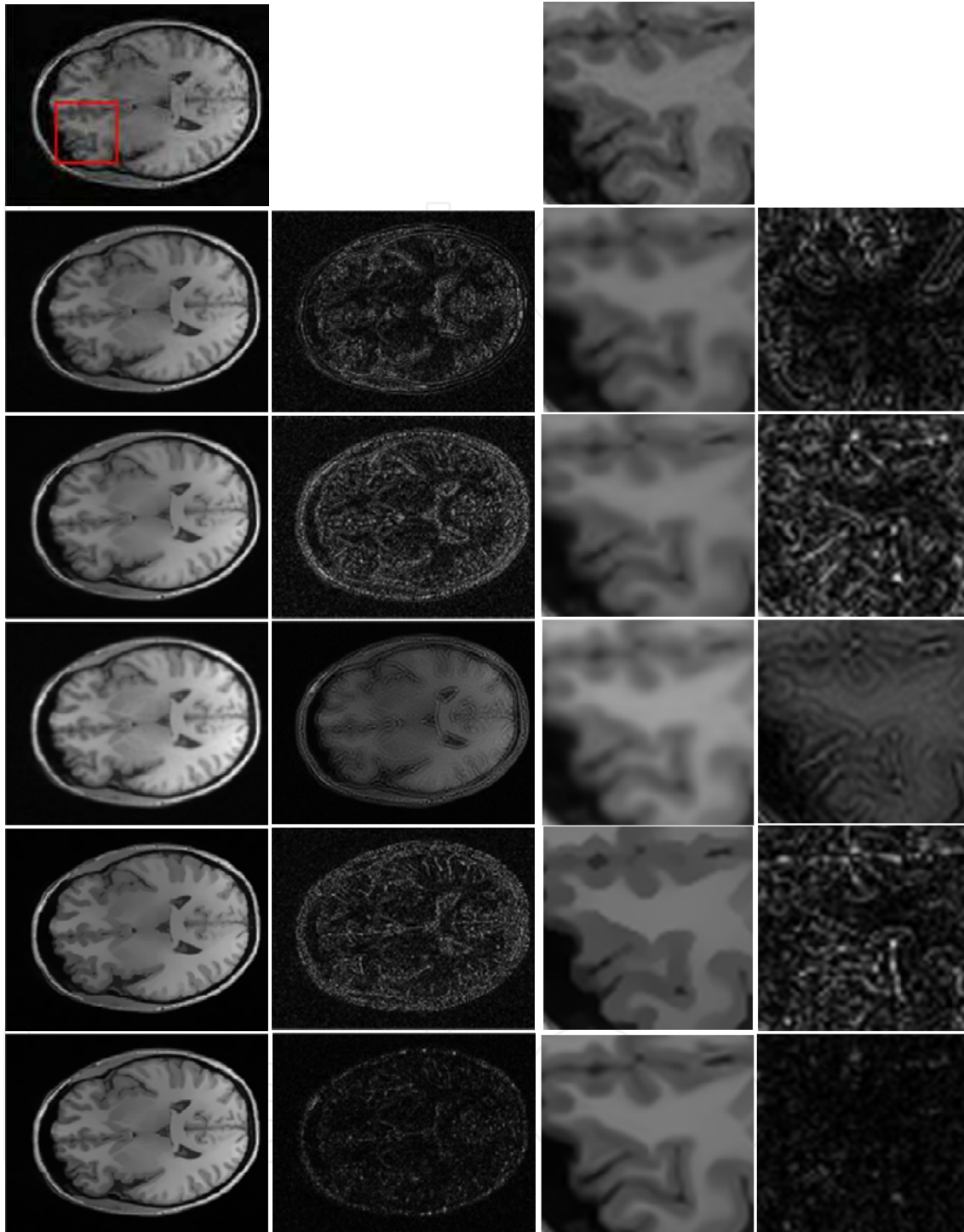


Fig. 9. Qualitative comparison of filtering results after using the different methods for a slice. The first column is the real brain image and the filtered results after using Wiener filter, wavelet filter, AD filter, bilateral filter and our method from the top to the bottom respectively. The second column is the corresponding residuals between the original image and the filtered image. Qualitative comparisons of ROIs are shown in the third and fourth columns. The third column shows the ROIs of real brain image, and the filtered results using Wiener filter, wavelet filter, AD filter, bilateral filter and our method from top to bottom respectively. The fourth column shows the corresponding residuals in ROIs between the original image and the filtered image.

## 4.2 Real MR brain data

Our filtering method also was applied to real T1 weighted MR images of the human brain. Fig. 9 illustrates the visual assessment of the filtered results of real T1-weighted MR brain images using the five different methods. By comparing the filtered results and corresponding residuals, it can easily be seen that Wiener filter makes image blurred and their residual in the whole image is almost the same except edges. Wavelet filter seems to introduce artifacts in the denoised image. AD filter erases small features and transforms image statistics due to its edge enhancement effect resulting in an unnatural image. And it can also be seen that bilateral filter and our method are excellent in reducing the noise, and enhancing the image contrast. But bilateral filter loses many small edges and features while our method preserves more of the details. The enlarged view of the region of interest (ROI) is also shown in Fig.9. It is evident that our method suppresses noise effectively while keeping more of the image details by comparing the two ROIs ( $50 \times 50$  voxels).

## 5. Conclusion

A wavelet domain filtering method based on the Radon transform for noise reduction in medical images was presented. We performed the Radon transform for input images, and based on our image model we validated that the Radon transform can improve the SNR and zero mean white noise has no effect on it. Wavelet analysis decomposes a signal into a hierarchy of scales ranging from the coarsest scale to the finest one. Orthogonal wavelet transforms have fewer coefficients at coarse scales, which prevents the transformed signal from correlated across the scales. Lack of a translation invariant makes filtering by orthogonal wavelet transforms exhibit visual artifacts. Therefore, we apply a 1D non-orthogonal wavelet transform along  $s$ , and use a threshold-based method to filter. We use a spatial correlation function to enhance significant structures and dilute noise, and then estimate the original noise variance from the first two scales. Dissimilar to traditional threshold methods that apply the same threshold to the wavelet coefficients in all scales, the proposed method provides an adaptive and robust threshold for every scale. The images in the Radon domain do not have more high-frequency parts or more edges than the corresponding images in the time domain, so our method for noise variance estimation works well. On the other side, inverse radon transform will introduce some artifacts [27]. Currently, our method produced promising results on a small segment of the image in additive Gaussian noise. Further work needs to be performed to shown if this technique is useful in multiplicative noise, on a larger wake image, and the wake detection problem.

Simulated brain MR image and real brain MR image images were used to validate our method. Wiener filter, wavelet filter, AD filter and bilateral filter were compared with our method. Our method performed better than the other methods in improving SNR and in preserving the key image details and features. The experimental results showed the superiority of the proposed method as it outperformed the traditional denoising methods. Our method can also be used in other medical imaging.

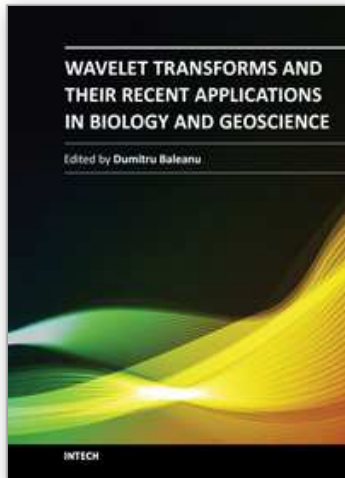
## 6. References

- [1] Xiaofeng Y, Baowei F. A wavelet multiscale denoising algorithm for magnetic resonance (MR) images. *Measurement Science and Technology*, 2011, 22 (2): 025803-025815.

- [2] Perona P, Malik J. Scale-space and edge detections using anisotropic diffusion. *IEEE Transactions on Pattern Analysis and Machine Intelligence*. 1990; 12: 629-39.
- [3] Samsonov A, Johnson C. Noise-adaptive nonlinear diffusion filtering of MR images with spatially varying noise levels. *Magnetic Resonance in Medicine*. 2004; 52: 798-806.
- [4] Wong W, Chung A. Trilateral filtering: a non-linear noise reduction technique for MRI. *International Society for Magnetic Resonance in Medicine*. 2004; 2218.
- [5] Tomasi C, Manduchi R. Bilateral filtering for gray and color images. *Sixth International Conference on Computer Vision*. 1998; 839-46.
- [6] Healy D M, Weaver J B. Two applications of wavelet transforms in magnetic resonance imaging. *IEEE Transactions on Information Theory* 1992; 38: 840-60.
- [7] Nowak R D. Wavelet-based Rician noise removal for magnetic resonance imaging. *IEEE Transactions on Image Processing* 1999; 8: 1408-19
- [8] Donoho D L, Johnstone I M. Ideal spatial adaptation by wavelet shrinkage. *Biometrika Trust* 1994; 81:425-455.
- [9] Quan P, Lei Z, Guanzhong D, Hongai Z. Two denoising methods by wavelet transform. *IEEE Transactions on Signal Processing* 1999; 47: 3401-06.
- [10] Paul B, Lei Z. Noise reduction for magnetic resonance images via adaptive multiscale products thresholding. *IEEE Transactions on Medical Imaging* 2003; 22: 1089-99.
- [11] Pizurica A, Philips W, Lemahieu I, Acheroy M. A versatile wavelet domain noise filtration technique for medical imaging. *IEEE Transactions on Medical Imaging* 2003; 22: 323-31.
- [12] Yansun X, Weaver J B, Healy D M, Jian L. Wavelet transform domain filters: a spatially selective noise filtration technique. *IEEE Transactions on Image Processing* 1994; 3:747-58.
- [13] Deng Z, Toshi H N. Medical Image Noise Reduction Using Radon Transform and Walsh List in Laplacian Pyramid Domain. *The 13th IEEE International Symposium on Consumer Electronics (ISCE2009)*. 2009; 756-760.
- [14] Ratnaparkhe V R , Manthalkar R R, Joshi Y V. Texture Characterization of CT Images Based on Ridgelet Transform. *ICGST-GVIP 2009*; 8: 43-50.
- [15] Anand C S, Sahambi J S. MRI denoising using bilateral filter in redundant wavelet domain. *TENCON 2008. IEEE Region 10 Conference 2008*; 1-6.
- [16] Mallat S G. A Theory for Multiresolution Signal Decomposition - the Wavelet Representation. *IEEE Transactions on Pattern Analysis and Machine Intelligence* 1989; 11: 674-93.
- [17] Mallat S, Zhong S. Complete signal representation with multiscale edges. *New York University, Institute of Fine Arts Library*. 1989.
- [18] Xiaofeng Y, Peng L, Xin Z, Zhengzhong B, Bo W. De-Noising of the Doppler Fetal Heart Rate Signal with Wavelet Threshold Filtering Based on Spatial Correlation. *Bioinformatics and Biomedical Engineering, 2007. ICBBE 2007. The 1st International Conference on*, 928-931, 6-8 July 2007
- [19] Delakis I, Hammad O, Kitney R I. Wavelet-based de-noising algorithm for images acquired with parallel magnetic resonance imaging (MRI). *Physics in Medicine and Biology* 2007; 52: 3741-51.
- [20] Yazgan B, Paker S, Kartal M. Image reconstruction with diffraction tomography using different inverse Radon transform algorithms. *Proceedings of the 1992 International Biomedical Engineering Days 1992*; 170-173

- [21] Nam-Yong L, Lucier B J. Wavelet methods for inverting the Radon transform with noisy data *IEEE Transactions on Image Processing*. 2001; 10: 79-94
- [22] Horbelt S, Liebling M, Unser M. Discretization of the radon transform and of its inverse by spline convolutions *IEEE Transactions on Medical Imaging*. 2002; 21: 363-376.
- [23] Kwan R K S, Evans A C, Pike G B. MRI simulation-based evaluation of image-processing and classification methods. *IEEE Transactions on Medical Imaging*. 1999; 18: 1085-97.
- [24] Xiaofeng Y, Baowei F. A multiscale and multiblock fuzzy c-means classification method for brain MR images. *Medical Physics*, 2011; 38 (6): 2879-2893.
- [25] Xiaofeng Y, Sechopoulos I, Baowei F. Automatic tissue classification for high-resolution breast CT images based on bilateral filtering. *Proc. SPIE 7962, 79623H* (2011); doi:10.1117/ 12.877881
- [26] Xiaofeng Y, Baowei F. A MR Brain Classification Method Based on Multiscale and Multiblock Fuzzy C-Means. *Bioinformatics and Biomedical Engineering, (iCBBE) 2011 5th International Conference on, 1-4, May 2011*
- [27] Xiaofeng Y, and Baowei F. A skull segmentation method for brain MR images based on multiscale bilateral filtering scheme. *Proc. SPIE 7623, 76233K* (2010); doi:10.1117/12.844677

IntechOpen



## **Wavelet Transforms and Their Recent Applications in Biology and Geoscience**

Edited by Dr. Dumitru Baleanu

ISBN 978-953-51-0212-0

Hard cover, 298 pages

**Publisher** InTech

**Published online** 02, March, 2012

**Published in print edition** March, 2012

This book reports on recent applications in biology and geoscience. Among them we mention the application of wavelet transforms in the treatment of EEG signals, the dimensionality reduction of the gait recognition framework, the biometric identification and verification. The book also contains applications of the wavelet transforms in the analysis of data collected from sport and breast cancer. The denoting procedure is analyzed within wavelet transform and applied on data coming from real world applications. The book ends with two important applications of the wavelet transforms in geoscience.

### **How to reference**

In order to correctly reference this scholarly work, feel free to copy and paste the following:

Xueling Zhu, Xiaofeng Yang, Qinwu Zhou, Liya Wang, Fulai Yuan and Zhengzhong Bian (2012). A Wavelet Multiscale De-Noising Algorithm Based on Radon Transform, Wavelet Transforms and Their Recent Applications in Biology and Geoscience, Dr. Dumitru Baleanu (Ed.), ISBN: 978-953-51-0212-0, InTech, Available from: <http://www.intechopen.com/books/wavelet-transforms-and-their-recent-applications-in-biology-and-geoscience/a-wavelet-multiscale-de-noising-algorithm-based-on-radon-transform>

**INTECH**  
open science | open minds

### **InTech Europe**

University Campus STeP Ri  
Slavka Krautzeka 83/A  
51000 Rijeka, Croatia  
Phone: +385 (51) 770 447  
Fax: +385 (51) 686 166  
[www.intechopen.com](http://www.intechopen.com)

### **InTech China**

Unit 405, Office Block, Hotel Equatorial Shanghai  
No.65, Yan An Road (West), Shanghai, 200040, China  
中国上海市延安西路65号上海国际贵都大饭店办公楼405单元  
Phone: +86-21-62489820  
Fax: +86-21-62489821

© 2012 The Author(s). Licensee IntechOpen. This is an open access article distributed under the terms of the [Creative Commons Attribution 3.0 License](#), which permits unrestricted use, distribution, and reproduction in any medium, provided the original work is properly cited.

IntechOpen

IntechOpen